Journal of Materials Chemistry A

ROYAL SOCIETY OF CHEMISTRY

PAPER

View Article Online
View Journal | View Issue

Cite this: J. Mater. Chem. A, 2020, 8, 10370

A three-dimensional interconnected V_6O_{13} nest with a V^{5+}-rich state for ultrahigh Zn ion storage†

Pingge He, ‡[a] Jiahao Liu,‡[a] Xudong Zhao,[a] Zhengping Ding,[b] Peng Gao [bc] and Li-Zhen Fan *[a]

Received 20th March 2020
Accepted 4th May 2020

DOI: 10.1039/d0ta03165h

rsc.li/materials-a

Aqueous zinc ion batteries (ZIBs) have attracted intensive attention due to their low cost, environmental friendliness and high safety. However, exploring suitable cathode materials and a deep understanding of their energy storage mechanisms remain a daunting challenge. In this work, a three-dimensional (3D) nest-like V_6O_{13} structure is grown on carbon cloth (CC) as a free-standing ZIB cathode. Such interconnected V_6O_{13} nanoneedles forming a 3D nest structure provide a large accessible surface area to the electrolyte and rapid channels for Zn^{2+} diffusion, and V_6O_{13} with a V^{5+}-rich state allows for more possibilities of multielectron reaction upon Zn (de)intercalation. As a result, an aqueous ZIB based on the V_6O_{13}/CC cathode and low-cost $ZnSO_4$ electrolyte shows an ultrahigh capacity of 520 mA h g^{-1} (at a current density of 0.5 A g^{-1}), desirable rate capability and cycle life (showing a stable capacity of 335 mA h g^{-1} over 1000 cycles). Moreover, the Zn^{2+} storage mechanism is deeply investigated based on experimental data and density functional theory simulation, and flexible solid-state ZIBs are established based on such a V_6O_{13}/CC cathode to reveal its high functional flexibility and excellent electrochemical performance, showing great potential applications in high-performance and safe electronic devices.

Introduction

Low-cost and high-safety energy storage systems are increasingly demanded due to the continuous requirements of power portable electronics and electrical vehicles.[1,2] During the past several decades, lithium ion batteries have been dominant in new-generation energy storage devices widely applied in various fields ranging from portable electronic devices to grid-scale energy storage.[3–6] However, the high cost, limited sources of lithium and particularly the safety issues originating from organic electrolytes severely limited the further development of lithium ion batteries. Recently, novel multivalent-ion battery systems based on aqueous electrolytes rather than organic electrolytes have been regarded as promising candidates for next-generation power supplies to meet the sustainable development of renewable energy in modern life.[7]

Among them, zinc ion batteries (ZIBs) have received intensive attention since zinc-metal anodes provide a high theoretical capacity (specific capacity of 819 mA h g^{-1}), a low working potential (−0.763 V *vs.* SHE) and relatively high stability in aqueous electrolytes,[8–10] showing preferable applications in high-performance aqueous batteries with environmental friendliness, low cost and high safety.[11] However, due to the large atomic mass (solvation sheath), strong positive polarity, and high charge/radius ratio of Zn^{2+}, the capability of cathode materials to accommodate Zn ions and the insertion/de-insertion kinetics are severely limited.[12] Thus, exploring novel cathode materials with appropriate crystal structure and fast Zn^{2+} diffusion channels remains an unmet challenge.

Currently, V-based oxides[13,14] particularly V_6O_{13} with wide-range oxidation states and metallic-like characters at room temperature[15,16] have been highly developed as ZIB cathodes, showing high capacity, good rate capability and desirable cycling stability.[17,18] Besides the open-framework crystal structure to provide available channels for easy intercalation of Zn ions, the high electronic conductivity at room temperature and high electrochemical activity of V_6O_{13} attributed to dual-valences of V^{5+} and V^{4+} endow it with great potential as a high-performance cathode material for ZIBs.[17] Nonetheless, the capacity and corresponding energy density are still far from enough to meet the practical requirements. Construction of three-dimensional (3D) nanostructured V_6O_{13} materials with large surface areas and short ion diffusion distances have been demonstrated to facilitate electrochemical kinetics, thus

[a]Beijing Advanced Innovation Center for Materials Genome Engineering, Institute of Advanced Materials and Technology, University of Science and Technology Beijing, Beijing 100083, China. E-mail: fanlizhen@ustb.edu.cn

[b]International Center for Quantum Materials, Electron Microscopy Laboratory, School of Physics, Peking University, Beijing 100871, China

[c]Collaborative Innovation Centre of Quantum Matter, Beijing 100871, China

† Electronic supplementary information (ESI) available: Preparation details, SEM images, XRD patterns, XPS spectra and Raman spectra. The calculated diffusion contribution and EIS. Calculated diffusion energy barriers. See DOI: 10.1039/d0ta03165h

‡ P. He and J. Liu contribute equally to this work.

improving the electrochemical performance.[19,20] Meanwhile, the capacity reflecting the Zn^{2+} storage ability of multi-valent oxide cathodes is essentially related to their valence states, which significantly affects the redox reactions and consequently influences the capacity of cathodes.[21] Thus, tuning of valence states in multivalent oxides with a controllable 3D nanostructure could provide an effective way to improve the electrochemical kinetics thus enhancing the electrochemical performance of ZIBs.

In this work, a 3D nest-like V_6O_{13} structure with a high-content V^{5+} state was designed and prepared on carbon cloth (CC) as a free-standing cathode for high-performance ZIBs. Such a nest structure with interconnected V_6O_{13} nanoneedles provides a large accessible surface area to the electrolyte and rapid channels for Zn ion diffusion. With the mixed vanadium states of V^{4+}/V^{5+}, the tunnel-like V_6O_{13} comprises alternate single and double vanadium oxide layers with shared corners, providing more active sites for ion storage. Additionally, the wide range of oxidation states of vanadium allows for the possibility of multielectron reaction upon Zn (de)intercalation.[16,17] Moreover, the high-content V^{5+} state contributes to a highly effective redox reaction. As a result, such V_6O_{13}/CC cathodes exhibit ultrahigh discharge capacity, good rate capability and desirable cycling stability. Moreover, density functional theory (DFT) simulation combined with experimental data deeply reveals the mechanism of Zn ion diffusion and storage based on such V^{5+}-rich V_6O_{13} cathode materials, and the practical applicability and functionality of such cathodes have been demonstrated through the assembly of flexible devices with outstanding electrochemical performance.

Experimental

Synthesis of the V^{5+}-rich V_6O_{13} nest on CC as a 3D free-standing cathode

Before the hydrothermal process, CC was treated with 1 M H_3PO_4 overnight at a temperature of 50 °C to make its surface hydrophilic (for details see ESI†). After that, the CC was rinsed with deionized water to remove the residual acid on its surface. Subsequently, 0.1945 g NH_4VO_3 was dissolved in a mixed solution (55 mL of deionized water and 5 mL of ethanol) with continuous stirring. Subsequently, 2 M HCl (1 mL) was added to adjust the pH value of the solution to 2. Adding HCl to adjust the pH value to 2 could be beneficial for the dissolution of NH_4VO_3 in the solvent, which would contribute to the uniform formation of a V^{5+}-rich V_6O_{13} nest on the CC surface. Then the mixed solution was poured into a Teflon-lined autoclave (100 mL) with treated CC in it and kept at 160 °C in an oven. To study the influence of hydrothermal duration on the product structure, the solution was kept for 2 h, 5 h and 10 h, respectively. After the hydrothermal process, the samples were annealed at 400 °C under Ar for 2 h to obtain the interconnected V^{5+}-rich V_6O_{13} nest on CC. The mass loading of V_6O_{13} on CC is measured to be approx. 1.5 mg cm^{-2}. For comparison, the mixed solution without addition of 2 M HCl was also prepared for the synthesis of well-balanced V_6O_{13} on CC.

Structural characterization

X-ray diffraction (XRD, a D/ruanx 2550PC, Japan) and X-ray photoelectron spectroscopy (XPS, Thermo Fisher, ESCALAB 250Xi) were employed to investigate the crystal structure and chemical bonding of the materials. Scanning electron microscopy (SEM, Hitachi S4800) and transmission electron microscopy were used to study the microstructure. The TEM, HRTEM, and STEM images and EDX maps were acquired on a FEI Tecnai G2 F20 equipped with an Oneview IS (Gatan) camera and Oxford X-MaxN TSR EDS detector at 200 kV. N_2 adsorption/desorption measurements were performed to investigate the porous nature of V_6O_{13}/CC.

Electrochemical property measurements

As-prepared free-standing V_6O_{13}/CC was directly used as a cathode without adding any binder and conductive additive. Zn electrodeposited on CC was used as an anode and the detailed preparation process is shown in the ESI.† The mass loading of Zn on CC is measured to be 2.5 mg cm^{-2}. The cells were assembled in air, which avoids the complicated assembly process and is applicable for larger-scale fabrication. A LAND 2001A battery system was employed to conduct the galvanostatic charge and discharge measurements. An electrochemical workstation (CHI660D) was used to record the cyclic voltammetry (CV) curves and to obtain electrochemical impedance spectra (EIS) by applying an AC amplitude of 5 mV in a frequency range between 100 kHz and 0.01 Hz.

Simulation details

The Zn ion diffusion and storage mechanism were deeply investigated through first-principles calculations based on density functional theory (DFT). All the calculations were performed using the Vienna *ab initio* simulation package (VASP).[22] The projector augmented[23] method with the Perdew–Burke–Ernzerhof (PBE)[24] functional was adopted in this work. The energy cutoff and *k*-point were set to 500 eV and $(3 \times 9 \times 3)$ for structural optimization and Zn^{2+} diffusion. The migration pathways and energy barriers of Zn ions diffusing in the V_6O_{13} structure were studied by climbing image-nudged elastic band (cNEB)[25] and BVEL[26] methods.

Results and discussion

The unique structure of nest-like V^{5+}-rich V_6O_{13} grown on CC current collectors is schematically shown in Fig. 1a. Macroscopically woven CC (as shown in the Fig. 1b inset), with gaps of several micrometers between two adjacent carbon fibers, offers a 3D, conductive, flexible current collector and alleviates volume expansion during the charge/discharge process. Subsequently, V_6O_{13} nanoneedles interconnect with each other forming a 3D nest-like structure on the CC surface, further increasing the accessible surface area to the electrolyte and provides enough space for the volumetric change of the electrode during the charge/discharge process. In such a V_6O_{13}/CC structure, CC as the current collector with high conductivity and V_6O_{13}/CC as the free-standing electrode without any binder

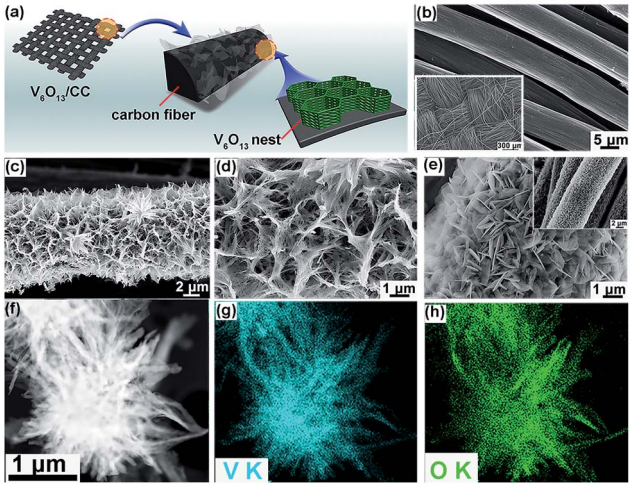

Fig. 1 (a) Schematic illustration of the 3D V_6O_{13} nest grown on CC for a high-performance ZIB cathode (the dotted circles in the image display the selected areas to be magnified). (b) Bare carbon fibers in CC (inset shows the woven characteristic of CC). (c) Uniform growth of the V_6O_{13} nest on carbon fibers at low magnification. (d) Interconnected V_6O_{13} nanoneedles forming a 3D nest-like structure. (e) Zn nanosheets with sharp edges on the carbon fiber surface (inset shows a uniform coverage of Zn nanosheets on carbon fibers). (f) High-angle annular dark field (HAADF) scanning TEM image of the V_6O_{13} nest. Elemental maps of (g) V and (h) O.

ensure quick electron transfer between the V_6O_{13} active material and the CC current collector.

For V_6O_{13} growth, the CC surface is relatively smooth with some grooves, which are beneficial for the subsequent nanomaterial loading (see Fig. 1b). After hydrothermal and calcination processes (the morphology and XRD patterns of the products before calcination have been provided in Fig. S1 and S2,† respectively), V_6O_{13} nanowires grow through various directions (spatially grow through x, y and z directions), interconnecting with each other to form a 3D nest-like structure (see Fig. 1c and d). The effects of hydrothermal duration on the V_6O_{13} structure are investigated and the SEM images of the products prepared under different hydrothermal durations are provided in Fig. S3.† Based on the SEM images, the formation of V_6O_{13} nest-like structures can be schematically shown in the ESI, Fig. S4,† which clearly illustrates the gradual formation process of 3D V_6O_{13} on the CC surface. Moreover, XRD of products calcined at air is provided in Fig. S5.† These results reveal that optimized experimental conditions exist for the V_6O_{13} nest-like structure with a hydrothermal time of 5 h and a calcination atmosphere of Ar.

For anode preparation, CC is also employed as the current collector for Zn nanosheet growth (for the experimental details see ESI†). As shown in Fig. 1e, after an electrodeposition time of 30 min (the electrodeposition process is shown in Fig. S6†), Zn nanosheets that are homogeneously deposited on the CC surface (see the inset in Fig. 1e) show numerous edges and a lateral size of approx. 1 μm (see Fig. 1e). The XRD shown in Fig. S7† confirms the presence of Zn on CC. However, if the electrodeposition duration is further prolonged, Zn nanosheets aggregate on the CC surface (as shown in Fig. S8†). Thus, the electrodeposition time of 30 min is chosen for the preparation of anodes. EDX maps in Fig. 1f–h show that such V_6O_{13} nests consist of V and O elements with uniform distribution among nanoneedles, providing a precondition for the superior performance of V_6O_{13}.

To further investigate the microstructure of the V_6O_{13} nest, different characterization methods are employed, and the results are shown in Fig. 2. The TEM image in Fig. 2a reveals an uneven surface nature of V_6O_{13} nanoneedles with many nanopores, which are clearly shown in the high-resolution TEM image in Fig. 2b. More details of TEM images have been provided in the ESI, Fig. S9.† The nanoporous structure has also been demonstrated by BET analysis in Fig. S10† and such nanopores are proved to be beneficial to the rapid transfer of charges/ions. The XRD pattern of V^{5+}-rich V_6O_{13}/CC in Fig. 2c shows two obvious peaks at 26.5° and 44.5° which are attributed to the (002) and (101) diffractions of graphite, and numerous weak peaks. Due to the intense diffraction peaks from the CC substrate, the diffraction peaks from V_6O_{13} in the XRD are hard to distinguish. Thus, V^{5+}-rich V_6O_{13} powder was collected for the XRD test and the result is shown in the Fig. 2c inset, which clearly shows diffraction peaks at 8.8°, 15.1°, 21.1°, 25.3°, 30.1°, 33.5°, 35.8°, 45.5°, 49.5°, 59.8°, 69.5° and 77.8°, which are indexed to the V_6O_{13} structure (PDF 89-0100).[27] Meanwhile, in the XRD pattern of V^{5+}-rich V_6O_{13}/CC, the diffraction peaks at $2\theta = 42°$ and 52° could have originated from the (204) and (220) plane diffractions of V_6O_{13}, and $2\theta = 31°$ and 34° might be attributed to the (400) and (310) plane diffractions of V_2O_5 (PDF 89-0612).

To reveal the V^{5+}-rich characteristic, XPS results of V 2p spectra of well-balanced V_6O_{13}/CC and V^{5+}-rich V_6O_{13}/CC have been shown in Fig. 2d and e, respectively (the detailed XPS of V^{5+}-rich V_6O_{13}/CC is shown in Fig. S11†). As shown in Fig. 2d, well-balanced V_6O_{13}/CC shows a fitted V 2p spectrum with two spin–orbit doublets, characteristic of V^{5+} (peaks at 517.5 eV and 525 eV)[27,28] and V^{4+} (peaks at 516.1 eV and 523.8 eV),[27,28]

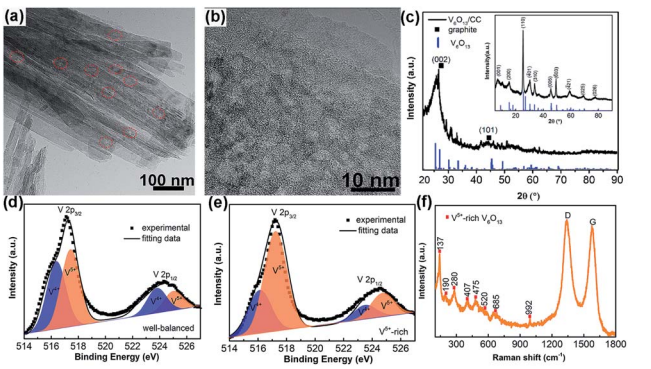

Fig. 2 (a) TEM image of V^{5+}-rich V_6O_{13} nanoneedles (the red circles indicate the uneven surface). (b) High-resolution TEM of a nanoneedle. (c) XRD of V^{5+}-rich V_6O_{13}/CC (inset shows the XRD of V_6O_{13} powder). (d) XPS with the V 2p spectrum of well-balanced V_6O_{13}/CC. (e) XPS with the V 2p spectrum of V^{5+}-rich V_6O_{13}/CC. (f) Raman result of V^{5+}-rich V_6O_{13}/CC.

indicating a multivalent nature of V_6O_{13}. However, for V^{5+}-rich V_6O_{13}/CC (see Fig. 2e), the peak intensity of V^{5+} is much higher than that of V^{4+}, and the intensity ratio of V^{5+} : V^{4+} can be calculated to be over 2 : 1, which is much higher than that of the traditional V_6O_{13} material (Fig. 2d). Such a V^{5+}-rich state could be attributed to the existence of some functional groups containing V^{5+} on the surface, which are generated during the synthesis process.

The Raman spectrum of V^{5+}-rich V_6O_{13}/CC shown in Fig. 2f further confirms the V^{5+}-rich character of V_6O_{13}. Besides predominant D and G peaks arising from the CC substrate, the product shows peaks at around 137, 190, 280, 407, 475, 520, 685 and 992 cm^{-1}, while typical peaks attributed to traditional V_6O_{13} at 836, 875 and 923 cm^{-1} have not appeared.[29] The strong peak at 137 cm^{-1} is attributed to the B_g symmetry and two peaks observed at 407 and 280 cm^{-1} are attributed to V–O bending vibrations. Meanwhile, the peaks at 680, and 520 cm^{-1} are related to the oscillations from the V–O stretching. The peak at 475 cm^{-1} originates from bonds of three coordinated O–V(3).[30] Notably, the peak at 992 cm^{-1} is related to the vanadyl-oxygen stretching mode (characteristic peak of V^{5+} in V_2O_5).[31] To eliminate the influence from the CC substrate, the Raman spectrum of V_6O_{13} powder is shown in Fig. S12,† and the result presents an obvious peak at 992 cm^{-1}, further confirming a strong V^{5+}-rich characteristic in such V_6O_{13}.

The electrochemical performance of V^{5+}-rich V_6O_{13} cathodes in 3 M $ZnSO_4$ aqueous electrolyte is systematically investigated and for comparison, the well-balanced V_6O_{13} material is also electrochemically characterized under the same conditions. Fig. 3a shows the comparative charge/discharge profiles (tested at 500 mA g^{-1}) of these two electrodes. For V^{5+}-rich V_6O_{13}, it shows two obvious charge (1.2 V) and discharge (1 V) voltage plateaus and exhibits a capacity of approximately 480 mA h g^{-1}. However, for well-balanced V_6O_{13}, only a capacity of 350 mA h g^{-1} can be achieved with charge voltage plateaus at approx. 0.6 V and 1.2 V and discharge voltage plateaus at 1 V and 0.55 V. The different charge/discharge curves between well-balanced V_6O_{13} and V^{5+}-rich V_6O_{13} cathodes could be attributed to the different reaction mechanisms. For well-balanced V_6O_{13} cathodes, the reaction involves the insertion/extraction process of Zn ion storage in V_6O_{13}. However, for the V^{5+}-rich V_6O_{13} cathode, during the charge/discharge process, the insertion/extraction process of Zn ion storage in V_6O_{13} occurred synchronously combined with the valence state transition of the V element, which will be discussed deeply in the later XRD and XPS results. Meanwhile, the significantly increased capacity of V^{5+}-rich V_6O_{13} confirms that the V^{5+}-rich state plays a critical role in improving the Zn ion storage ability of V_6O_{13} cathodes. Moreover, Fig. 3b displays galvanostatic charge/discharge curves of the V^{5+}-rich V_6O_{13} over 3 cycles tested at 500 mA g^{-1}, showing that the V^{5+}-rich V_6O_{13}/CC cathode exhibits a stable discharge capacity of 520 mA h g^{-1} at 0.5 A g^{-1}, which is much higher than those of the state-of-the-art V-based ZIB cathode (falling in a range of 213 to 423 mA h g^{-1}, shown in Table S1†). To eliminate the influence from the CC substrate, the electrochemical performance of the bare CC electrode is provided in Fig. S13† (the capacity from the CC substrate could be negligible). The significant improvements in capacity could be attributed to the unique 3D nest structure and V^{5+}-rich state of V_6O_{13}. As shown in Fig. 3c, the V^{5+}-rich V_6O_{13}/CC//Zn/CC battery exhibits an outstanding rate capability, exhibiting discharge capacities of 234 mA h g^{-1} at a current density of up to 15 A g^{-1}. Furthermore, the capacity recovers to approx. 510 mA h g^{-1} when the current density switches to 0.5 A g^{-1}, indicating a high reversibility of the intercalation/de-intercalation process.

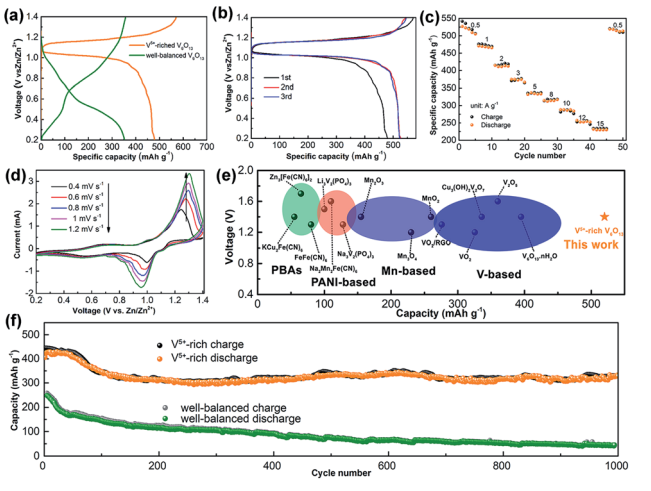

Fig. 3 Electrochemical performance of the V^{5+}-rich V_6O_{13}/CC//Zn/CC battery in 3 M $ZnSO_4$ electrolyte: (a) comparative charge/discharge profiles of well-balanced V_6O_{13} and V^{5+}-rich V_6O_{13} cathodes for the first cycle at 0.5 A g^{-1}. (b) Charge/discharge profiles of V^{5+}-rich V_6O_{13} cathodes. (c) Rate capability at various current densities. (d) CV curves at scan rates ranging from 0.4 to 1.2 mV s^{-1}. (e) Specific capacity *versus* voltage of different electrode materials for Zn^{2+} storage. (f) Comparative cycling stabilities of well-balanced V_6O_{13} and V^{5+}-rich V_6O_{13} electrodes at 2 A g^{-1} over 1000 cycles.

Moreover, CV curves were measured at different scan rates from 0.4 to 1.2 mV s^{-1} to understand the kinetics of the Zn^{2+} diffusion process. As shown in Fig. 3c, all CV curves display two obvious redox peaks, which are consistent with the voltage plateaus in Fig. 3b. The relationship between the anodic and cathodic peak currents and the scan rate is shown in Fig. S14a,† indicating that the redox reaction is a diffusion-controlled process. Moreover, the diffusion behavior is quantitatively evaluated based on CV results at different scan rates according to the following equation:[6,32]

$$I(V) = k_1 v + k_2 v^{1/2} \quad (1)$$

where v is the sweep rate, $k_1 v$ represents the capacitive contribution and $k_2 v^{1/2}$ is the Zn^{2+} insertion contribution. Therefore, the capacitive and diffusion contribution to the current at a specific voltage can be determined through calculating k_1 and k_2 values. As shown in Fig. S14b,† when the scan rate increases from 0.4 of 1.2 mV s^{-1}, the diffusion process contributes approx. 84.3%, 82.4%, 80%, 77.5% and 75.9% of the whole stored charge, indicating that the capacitive process contributes approx. 15.7%, 17.6%, 20%, 22.5% and 24.1% of the whole stored charge. Taking the CV curve at 1.2 mV s^{-1} as a typical

example, the fitted capacitive-based CV has been plotted and the result has been provided in the ESI, Fig. S15.† Moreover, 75.9% of the stored charge comes from the diffusion process even at a high scan rate of 1.2 mV s^{-1}, which demonstrates the high diffusion contribution of the V^{5+}-rich V_6O_{13} cathode during the charge/discharge process.

For a battery system, high capacity combined with high voltage is critical for achieving high energy density ($E = 1/2CV^2$). Fig. 3d presents the output voltages *versus* discharge capacities of V^{5+}-rich V_6O_{13} cathodes and those reported in the literature. Generally, some materials provide a high output voltage with a low discharge capacity (*e.g.* PBA- and PANI-based materials),[33,34] while others offer a high capacity but give a low discharge voltage (Mn- and V-based materials).[34,35] V^{5+}-rich V_6O_{13} cathodes prepared in this work exhibit an ultrahigh capacity and meanwhile maintain a desirable output voltage, which show great superiority among all-of-the-state ZIB cathode materials. Comparative cycling stabilities of V^{5+}-rich V_6O_{13} and well-balanced V_6O_{13} were evaluated at 2 A g^{-1}. Fig. 3e shows that the capacity of V^{5+}-rich V_6O_{13} undergoes a gradual decrease during the first 200 cycles and a slight increase before being stable at a capacity of approx. 335 mA h g^{-1} (with 85.3% capacity retention at the 1000th cycle). The cycling stability (the capacity retention is not that high) in this work is not as outstanding as we expected, but the capacity of 335 mA h g^{-1} over 1000 cycles is comparable to those of contemporary ZIB cathodes (see ESI, Table S1†). Notably, the slight increase in capacity during the cycling could be attributed to the activation of electrodes, which has also been observed in other aqueous batteries.[36–38] In a sharp contrast, the well-balanced V_6O_{13} electrode experiences a continuous decrease in capacity with a capacity of only 53.4 mA h g^{-1} at the 1000th cycle (with 25% capacity retention). The remarkably improved cycling stability of V^{5+}-rich V_6O_{13} electrodes further demonstrates that such a 3D nest-like structure with a V^{5+}-rich state is beneficial to the electrochemical kinetics of Zn ion diffusion. Moreover, the cycling performance of the V^{5+}-rich V_6O_{13} cathode at a low current density is shown in Fig. S16.† Additionally, the comparative EIS spectra of well-balanced V_6O_{13} and V^{5+}-rich V_6O_{13} cathodes are shown in Fig. S17 and S18,† respectively, indicating a relatively lower internal resistance and charge transfer resistance of V^{5+}-rich V_6O_{13}. Notably, the microstructure and morphology of V^{5+}-rich V_6O_{13}/CC electrodes after the 1000-cycling test show few changes that nest-like V_6O_{13} nanoneedles still uniformly and densely cover the CC surface (see Fig. S19†), revealing high structural stability of such hybrid structures, which could contribute to the enhanced cycling stability of such cathode materials. Moreover, high stability of the Zn anode during cycling is essential for the practical applications of ZIBs.[39,40] SEM images of Zn/CC after cycling have been provided in Fig. S20,† suggesting that few Zn dendrites emerge during the cycling process.

To investigate the Zn ion storage mechanism of such V^{5+}-rich V_6O_{13} cathodes, *ex situ* XRD and XPS were used to investigate the crystal structure and valence state evolutions of the V_6O_{13} cathode (using Ti foil as the current collector to avoid the influence from the CC substrate) under different charge/discharge states. As shown in Fig. 4a, peaks at around 35.1°, 38.4° and 40.2° which originate from the Ti (100), (002) and (101) plane diffractions remain at the same position, while other peaks show significant position shifts with the same tendency. The magnified XRD (see the rightward image in Fig. 3a) clearly shows that the peak at 25.5°, which is attributed to the (110) plane diffraction of V_6O_{13}, firstly shifts to a smaller angle (larger *d*-spacing) during the discharge process while it moves to a larger angle (smaller *d*-spacing) during the charge process. Such peak shifts indicate the intercalation of Zn ions into V_6O_{13} during the discharge process and the de-intercalation of Zn ions during the charge process with high reversibility, and such an increased *d*-spacing reveals a large accommodation for Zn ions, which further confirms the high capacity of V_6O_{13} cathodes. Moreover, the SEM images and TEM-EDX maps of such V_6O_{13} cathodes after the discharge process have been provided in the ESI, Fig. S21 and S22.† The TEM-EDX mapping shows the presence and uniform distribution of Zn among V_6O_{13} nanoneedles, further confirming the intercalation of Zn ions into V_6O_{13} during the discharge process.

XPS results of V_6O_{13} after discharge to 0.2 V and charge to 1.4 V have been shown in Fig. 4b–e. From the Zn 2p spectrum in Fig. 4b, after discharge to 0.2 V, intense peaks attributed to the Zn $2p_{3/2}$ and $2p_{1/2}$ orbitals arise which indicates the presence of the Zn element in V_6O_{13} after discharging to 0.2 V, while the peaks become much weaker after charging to 1.4 V, which

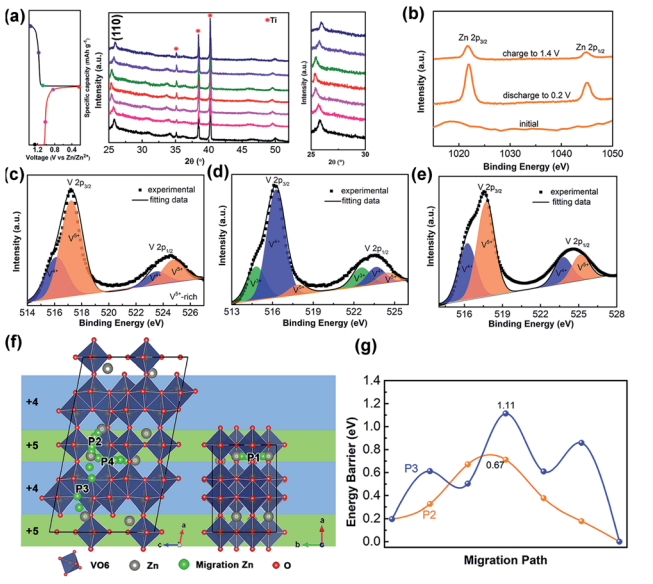

Fig. 4 (a) *Ex situ* XRD investigation (right-side) of V^{5+}-rich V_6O_{13} at various charge/discharge states (left-side). The colors of the XRD patterns correspond to the marked point in the charge/discharge curve. *Ex situ* XPS investigation of V^{5+}-rich V_6O_{13} at various charge/discharge states: (b) Zn 2p spectra; (c) V 2p spectrum of the pristine cathode; (d) V 2p spectrum of the cathode after charging to 1.4 V; (e) V 2p spectrum of the cathode after discharging to 0.2 V. Simulation study of the Zn ion diffusion process: (f) various diffusion pathways of Zn ions among such V_6O_{13} structures. (g) Calculated diffusion energy barriers for paths of P2 and P3 in (f).

indicates that most of the Zn would reversibly de-intercalate during the charging process, and also little Zn remains in the cathode structure. Furthermore, as shown in the V 2p spectra (see Fig. 4c–e), the original V_6O_{13} cathode consists of V^{4+} and V^{5+} mixed valence states (see Fig. 4c) with a high proportion of V^{5+}. However, after discharge to 0.2 V, the intensity of the V^{5+} valence state sharply decreases, and the proportion of V^{4+} increases and meanwhile a valence state of V^{3+} appears (see Fig. 4d). The conversion of the valence state is attributed to the Zn intercalation and corresponding redox reactions. The high-proportion V^{5+} in the original V_6O_{13} material is preferable to improve the redox process, consequently contributing to high capacity of the cell. When the cell is charged to 1.4 V, V^{4+} and V^{5+} valence states are recovered in the V_6O_{13} cathode (see Fig. 4e). The XRD and XPS results suggest reversible Zn^{2+} insertion/extraction into/from the electrode during the charge/discharge process.

Moreover, to deeply elucidate the Zn ion diffusion behavior in such cathode materials, DFT simulations based on optimized geometries of Zn-intercalated V_6O_{13} were carried out. As shown in Fig. 4f, considering the geometric symmetry of the crystal structure, two different kinds of Zn-intercalated positions are present in the V_6O_{13} structure with corresponding four various Zn ion diffusion pathways (P1–P4), where P1 is the diffusion way between spatially symmetric Zn ions along the *b* axis, P4 is the pathway between asymmetric Zn ions along the *c* axis, while P2 and P3 are pathways between Zn ions in different intercalation positions (asymmetric position) along the *a* axis. Zn ions could diffuse along these three axes but the energy barriers along *b* and *c* axes (P1 and P4, see Fig. S23†) are relatively higher than those along the *a* axis (P2 and P3, see Fig. 4g), indicating that Zn ions prefer to diffuse along the *a* axis in the V_6O_{13} structure. Moreover, in the crystal structure, V (4^+) and V (5^+) are alternately stacked in layers (see Fig. 4f, blue region represents the V^{4+} area and the green one shows the V^{5+} area). As shown in Fig. 4g, the energy barrier near the V^{5+} area (P2) is much lower than that near the V^{4+} area (P3), suggesting that the V^{5+}-rich state is beneficial for quick diffusion of Zn ions in the V_6O_{13} structure, which further demonstrates the superior electrochemical performance of V^{5+}-rich V_6O_{13} cathodes.

Inspired by the outstanding performance of the V^{5+}-rich V_6O_{13} cathode in aqueous electrolytes, a flexible ZIB system is built up (see Fig. 5a) through using free-standing V_6O_{13}/CC as the cathode, Zn/CC as the anode and $ZnSO_4$/PVA as the electrolyte and separator (for preparation details see ESI†). The electrochemical performance of such flexible cells is systematically investigated. As shown in Fig. 5b, the flexible device exhibits a discharge capacity of approx. 245 mA h g^{-1} at 0.5 A g^{-1}, which could be further improved through optimizing the mass loading of the active material and adjusting sol–gel electrolyte properties (*e.g.* the kind of salt and polymer, and the concentration of salt). As shown in Fig. 5c, the flexible device shows a desirable rate performance, exhibiting discharge capacities of approx. 140 mA h g^{-1} at 10 A g^{-1}. Furthermore, the capacity recovers to approx. 240 mA h g^{-1} when the current density switches to 0.5 A g^{-1}, indicating a high reversibility of the intercalation/de-intercalation process. Additionally, the EIS

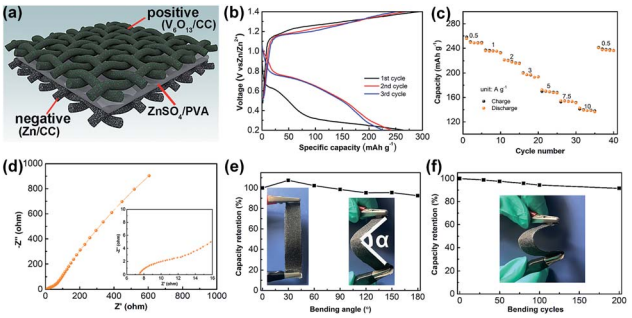

Fig. 5 The electrochemical performance of the flexible ZIB: (a) schematic of the battery structure. (b) Charge/discharge profiles at 0.5 A g^{-1} for the first three cycles. (c) Rate capability under various currents. (d) EIS recorded at an AC amplitude of 5 mV (the inset shows the magnified image). (e) Capacity retentions under different bending angles. (f) Capacity retentions over different bending cycles.

in Fig. 5d reveals a low internal resistance of 7.4 Ω and a low charge transfer resistance of 6.5 Ω of the flexible ZIB.

High elasticity and outstanding durability are critical factors for batteries applied in flexible/wearable and portable electronics in modern life. To meet the requirements of flexible batteries in practical applications, galvanostatic charge/discharge profiles of the batteries under various bending angles are obtained at 2 A g^{-1} and the resulting capacity retention according to different bending states is presented in Fig. 5e. The discharge capacity experiences few fluctuations even when the bending angle is up to 180° (with a capacity retention of 93.5%), demonstrating high flexibility of the flexible ZIB battery. Moreover, the cyclic bending stability of the flexible ZIB battery is shown in Fig. 5f through measuring the discharge capacity at 2 A g^{-1} of the battery after various bending cycles. The flexible device maintains a high capacity retention of over 90% even when the device is bent over 200 cycles. All the results reveal that the ZIB battery based on the V^{5+}-rich V_6O_{13}/CC cathode and PVA electrolyte system exhibits excellent structural flexibility and durability, indicating its great promise as a flexible power supply in electronic devices.

Conclusion

In summary, 3D V_6O_{13} nests with a V^{5+}-rich state were directly grown on a CC substrate as high-performance cathodes for ZIBs. Benefiting from the unique 3D interconnected structure and high content of the V^{5+} state, such V_6O_{13}/CC cathodes exhibit an ultrahigh discharge capacity of 520 mA h g^{-1} at 0.5 A g^{-1}, desirable rate capability and long cycle life with a stable capacity of approx. 335 mA h g^{-1} over 1000 cycles. The Zn ion diffusion and storage mechanism were deeply investigated based on experimental data combined with DFT simulations, revealing various quick pathways for Zn ion diffusion with a low energy barrier, which further confirms the superiority of such a V^{5+}-rich V_6O_{13} cathode for rapid Zn ion diffusion. Moreover, such flexible and free-standing V_6O_{13}/CC cathodes endow ZIBs with high safety, high flexibility and durability in practical applications, showing great promise in high-

performance flexible smart electronics. The achieved results indicate that the tuning of the valence state and construction of the 3D network structure on cathode materials provide a highly effective way to enhance the electrochemical performance of electrodes, which is particularly well-suited for practical implementation in high-performance batteries.

Conflicts of interest

There are no conflicts to declare.

Acknowledgements

The authors gratefully acknowledge the financial support from the Beijing Natural Science Foundation (2204086), the Post-doctoral Science Fund of China (214060), the University Basic Research Fund of China (06500105), the National Natural Science Foundation of China (51532002, 51872027 and 51802297), the Beijing Natural Science Foundation (L172023), the National Basic Research Program of China (2017YFE0113500), and the Key R&D Program of Guangdong Province (2018B030327001, 2018B010109009).

Notes and references

1 D. Larcher and J.-M. Tarascon, *Nat. Chem.*, 2015, **7**, 19.
2 G. Xiong, P. He, B. Huang, T. Chen, Z. Bo and T. S. Fisher, *Nano Energy*, 2017, **38**, 127–136.
3 P. He, K. Zhao, B. Huang, B. Zhang, Q. Huang, T. Chen and Q. Zhang, *J. Mater. Sci.*, 2018, **53**, 4482–4493.
4 V. Etacheri, R. Marom, R. Elazari, G. Salitra and D. Aurbach, *Energy Environ. Sci.*, 2011, **4**, 3243–3262.
5 G. L. Zhu, C. Z. Zhao, J. Q. Huang, C. He, J. Zhang, S. Chen, L. Xu, H. Yuan and Q. Zhang, *Small*, 2019, **15**, 1805389.
6 P. He, Z. Ding, X. Zhao, J. Liu, S. Yang, P. Gao and L.-Z. Fan, *Inorg. Chem.*, 2019, **58**, 12724–12732.
7 D. Selvakumaran, A. Pan, S. Liang and G. Cao, *J. Mater. Chem. A*, 2019, **7**, 18209–18236.
8 G. Fang, J. Zhou, A. Pan and S. Liang, *ACS Energy Lett.*, 2018, **3**, 2480–2501.
9 B. Tang, L. Shan, S. Liang and J. Zhou, *Energy Environ. Sci.*, 2019, **12**, 3288–3304.
10 K. Sada, B. Senthilkumar and P. Barpanda, *J. Mater. Chem. A*, 2019, **7**, 23981–23988.
11 S. Guo, S. Liang, B. Zhang, G. Fang, D. Ma and J. Zhou, *ACS Nano*, 2019, **13**, 13456–13464.
12 F. Wang, O. Borodin, T. Gao, X. Fan, W. Sun, F. Han, A. Faraone, J. A. Dura, K. Xu and C. Wang, *Nat. Mater.*, 2018, **17**, 543.
13 S. Guo, G. Fang, S. Liang, M. Chen, X. Wu and J. Zhou, *Acta Mater.*, 2019, **180**, 51–59.
14 M. Yan, P. He, Y. Chen, S. Wang, Q. Wei, K. Zhao, X. Xu, Q. An, Y. Shuang and Y. Shao, *Adv. Mater.*, 2018, **30**, 1703725.
15 W. Meng, R. Pigliapochi, P. M. Bayley, O. Pecher, M. W. Gaultois, I. D. Seymour, H.-P. Liang, W. Xu, K. M. Wiaderek and K. W. Chapman, *Chem. Mater.*, 2017, **29**, 5513–5524.
16 L. Shan, J. Zhou, W. Zhang, C. Xia, S. Guo, X. Ma, G. Fang, X. Wu and S. Liang, *Energy Technol.*, 2019, **7**, 1900022.
17 J. Shin, D. S. Choi, H. J. Lee, Y. Jung and J. W. Choi, *Adv. Energy Mater.*, 2019, **9**, 1900083.
18 F. Liu, Z. Chen, G. Fang, Z. Wang, Y. Cai, B. Tang, J. Zhou and S. Liang, *Nano-Micro Lett.*, 2019, **11**, 25.
19 Y.-L. Ding, Y. Wen, C. Wu, P. A. van Aken, J. Maier and Y. Yu, *Nano Lett.*, 2015, **15**, 1388–1394.
20 S. Wang, J. Qin, Y. Zhang, F. Xia, M. Liu, H. Chen, M. Al-Mamun, P. Liu, R. Rigway and G. Shi, *Energy Technol.*, 2019, 1801041.
21 L. Ma, S. Chen, H. Li, Z. Ruan, Z. Tang, Z. Liu, Z. Wang, Y. Huang, Z. Pei and J. A. Zapien, *Energy Environ. Sci.*, 2018, **11**, 2521–2530.
22 G. Kresse and J. Furthmüller, *Comput. Mater. Sci.*, 1996, **6**, 15–50.
23 G. Kresse and D. Joubert, *Phys. Rev. B: Condens. Matter Mater. Phys.*, 1999, **59**, 1758.
24 J. P. Perdew, K. Burke and M. Ernzerhof, *Phys. Rev. Lett.*, 1996, **77**, 3865.
25 G. Henkelman, B. P. Uberuaga and H. Jónsson, *J. Phys. Chem.*, 2000, **113**, 9901–9904.
26 M. Sale and M. Avdeev, *J. Appl. Crystallogr.*, 2012, **45**, 1054–1056.
27 Z. Huang, H. Zeng, L. Xue, X. Zhou, Y. Zhao and Q. Lai, *J. Alloys Compd.*, 2011, **509**, 10080–10085.
28 J. Wu, W. Huang, Q. Shi, J. Cai, D. Zhao, Y. Zhang and J. Yan, *Appl. Surf. Sci.*, 2013, **268**, 556–560.
29 C. Julien, G. Nazri and O. Bergström, *Phys. Status Solidi B*, 1997, **201**, 319–326.
30 C. Zhang, Q. Yang, C. Koughia, F. Ye, M. Sanayei, S.-J. Wen and S. Kasap, *Thin Solid Films*, 2016, **620**, 64–69.
31 P. Liu, K. Bian, K. Zhu, Y. Xu, Y. Gao, H. Luo, L. Lu, J. Wang, J. Liu and G. a. Tai, *ACS Appl. Mater. Interfaces*, 2017, **9**, 17002–17012.
32 T. C. Liu, W. Pell, B. Conway and S. Roberson, *J. Electrochem. Soc.*, 1998, **145**, 1882–1888.
33 L. Zhang, L. Chen, X. Zhou and Z. Liu, *Adv. Energy Mater.*, 2015, **5**, 1400930.
34 X. Guo, J. Zhou, C. Bai, X. Li, G. Fang and S. Liang, *Mater. Today Energy*, 2020, **16**, 100396.
35 X. Dai, F. Wan, L. Zhang, H. Cao and Z. Niu, *Energy Storage Materials*, 2019, **17**, 143–150.
36 M. Yan, P. He, Y. Chen, S. Wang, Q. Wei, K. Zhao, X. Xu, Q. An, Y. Shuang and Y. Shao, *Adv. Mater.*, 2017, **30**, 1703725.
37 Q. Pang, C. Sun, Y. Yu, K. Zhao, Z. Zhang, P. M. Voyles, G. Chen, Y. Wei and X. Wang, *Adv. Energy Mater.*, 2018, **8**, 1800144.
38 B. Tang, G. Fang, J. Zhou, L. Wang, Y. Lei, C. Wang, T. Lin, Y. Tang and S. Liang, *Nano Energy*, 2018, **51**, 579–587.
39 X. Xie, S. Liang, J. Gao, S. Guo, J. Guo, C. Wang, G. Xu, X. Wu, G. Chen and J. Zhou, *Energy Environ. Sci.*, 2020, **13**, 503.
40 C. Li, X. Shi, S. Liang, X. Ma, M. Han, X. Wu and J. Zhou, *Chem. Eng. J.*, 2020, **379**, 122248.

